RESEARCH ARTICLE
SPACE PHYSICS

Earth and Planetary Physics
9: 29–38, 2025
doi: 10.26464/epp2024044

An investigation on the wind profiles and gravity wave dynamics in MLT region based on the meteor radars from the Meridian Project

Tai Liu[1], Zhe Wang[1], MengXi Shi[1], Willie Soon[2,3], and ShiCan Qiu[1]*

[1]Department of Geophysics, College of the Geology Engineering and Geomatics, Chang'an University, Xi'an 710054, China;

[2]Center for Environmental Research and Earth Sciences (CERES), Salem, MA 01970, USA;

[3]Institute of Earth Physics and Space Science (ELKH EPSS), 9400, Sopron, Hungary

Key Points:

- The 2012–2022 meteor radar observations from the Meridian Project's Mohe Station in Heilongjiang and Zuoling Station in Wuhan provide a rare opportunity to study the long-term changes in the MLT region.
- The inversion of the meteor radar data reveals the coupling relationship and long-term change characteristics of the horizontal wind field, gravity wave disturbance variance and momentum flux.
- Lomb–Scargle analysis of the horizontal wind field, gravity wave disturbance variance, and gravity wave fluctuation fluxes reveals that their power spectral densities at 12-month and 6-month periods show an increase–decrease–re-increase pattern with increasing altitude.

Citation: Liu, T., Wang, Z., Shi, M. X., Soon, W., and Qiu, S. C. (2025). An investigation on the wind profiles and gravity wave dynamics in MLT region based on the meteor radars from the Meridian Project. *Earth Planet. Phys.*, *9*(1), 29–38. http://doi.org/10.26464/epp2024044

Abstract: The meteor radar can detect the zenith angle, azimuth, radial velocity, and altitude of meteor trails so that one can invert the wind profiles in the mesosphere and low thermosphere (MLT) region, based on the Interferometric and Doppler techniques. In this paper, the horizontal wind field, gravity wave (GW) disturbance variance, and GW fluxes are analyzed through the meteor radar observation from 2012–2022, at Mohe (53.5°N, 122.4°E) and Zuoling (30.5°N, 114.6°E) stations of the (Chinese) Meridian Project. The Lomb–Scargle periodogram method has been utilized to analyze the periodic variations for time series with observational data gaps. The results show that the zonal winds at both stations are eastward dominated, while the meridional winds are southward dominated. The variance of GW disturbances in the zonal and meridional directions increases gradually with height, and there is a strong pattern of annual variation. The zonal momentum flux of GW changes little with height, showing weak annual variation. The meridional GW flux varies gradually from northward to southward with height, and the annual periodicity is stronger. For both stations, the maximum values of zonal and meridional wind occur close to the peak heights of GW flux, with opposite directions. This observational evidence is consistent with the filtering theory. The horizontal wind velocity, GW flux, and disturbance variance of the GW at Mohe are overall smaller than those at Zuoling, indicating weaker activities in the MLT at Mohe. The power spectral density (PSD) calculated by the Lomb–Scargle periodogram shows that there are 12-month period and 6-month period in horizontal wind field, GW disturbance variance and GW flux at both stations, and especially there is also a 4-month cycle in the disturbance variance. The PSD of the 12-month and 6-month cycles exhibits maximum values below 88 km and above 94 km.

Keywords: meteor radar; wind field; gravity wave; Lomb–Scargle method

1. Introduction

The upper mesosphere and lower thermosphere (MLT) region of 80–100 km is a key connection region between outer space and lower atmosphere. The detection of wind profiles and gravity wave (GW) activities in MLT can help us better understand the structure of the middle and upper atmosphere (Jiang GY et al., 2005; Zhang RJ et al., 2022). The meteor radar is an important tool for detecting long-term changes in the MLT region, based on its advantages of low cost, continuous measurement, and all-weather detection (Hao XJ et al., 2023). The Interferometric and Doppler technologies are utilized to detect and deduce the zenith angle, azimuth angle, radial velocity, and height of meteor trails around the heights of 70–110 km, and then inverted to estimate the horizontal wind field (Hocking et al., 2001; Chen JS et al., 2016). The GW disturbance variance and GW momentum flux can be further derived through combining the Dual–Beam method with the Composite Day method (Hocking, 2005; Andrioli et al., 2013).

Around 2002, the first all-sky meteor radar in China was built at Wuhan (30.5°N, 114.2°E), followed by the stations in Kunming

First author: T. Liu, 2021126009@chd.edu.cn
Correspondence to: S. C. Qiu, scq@ustc.edu.cn
Received 30 MAR 2024; Accepted 17 JUN 2024.
First Published online 04 AUG 2024.

(25.6°N, 103.8°E), Mohe (53.5°N, 122.4°E), Beijing (40.3°N, 116.2°E), Langfang (39.4°N, 116.7°E), and Sanya (18.4°N, 109.6°E) (Xiong JG et al., 2003; Yang JF et al., 2017). In order to verify the accuracy of the horizontal wind field retrieved by the meteor radar, the meteor radar observations are often compared with the results from other radars at nearby stations (Fang X et al., 2013; Hao XJ et al., 2023). The horizontal wind field from November 2013 to December 2014 retrieved by two meteor radars and one Medium Frequency (MF) radar at Kunming station shows that the inversion results of the three radars at 80–90 km are close to each other, with small errors (Hao XJ et al., 2023). The zonal wind profiles retrieved by the meteor radar at Wuhan and the temperature/wind (T/W) lidar at Hefei have the same variation trend, both showing zonal wind with downward propagation at 90–105 km (Fang X et al., 2013). Observations of the wind field by meteor radar, sodium lidar and MF radar in Hawaii show that when the wind speed is small with slight variation, the horizontal wind fields observed by the three radars are all in good agreements (Gu SY et al., 2013).

Observations from April 2014 to December 2023 by the meteor radar at Mengcheng (33.4°N, 116.5°E) station show that the MLT region was characterized by eastward wind in summer and westward wind in winter above 84 km, but eastward wind in winter and westward wind in spring below 84 km (Yi W et al., 2023). The meridional wind was northward in winter and southward in summer from 76 km to 100 km (Yi W et al., 2023). The zonal wind in 2016 at Beijing station was dominated by westward wind, and the meridional wind alternated significantly between southward and northward (Zhang RJ et al., 2022). Chen JS et al. (2016) validated the inversion method for GW disturbance variance and momentum flux proposed by Hocking (2005), based on the observations at Kunming station in September 2014. The results showed that the inversion method proposed by Hocking was feasible within the appropriate sampling intervals (Chen JS et al., 2016).

In this paper, we study the long-term changes of horizontal wind field, GW disturbance variance and momentum flux with meteor radar observation from 2011–2022 at Mohe and Zuoling stations. Over a 2-hour period, at least 6–10 meteors per 3 km are needed to invert the horizontal wind field (Vincent et al., 2010), and more than 30 are required for the calculation of the GW momentum flux (Fritts et al., 2012a, b). The periodicity of the parameters could be analyzed in combination with the Lomb–Scargle power spectrum method (Lomb, 1976; Scargle, 1982; Horne and Baliunas, 1986).

2. Seismotectonic Setting

2.1 Horizontal Wind Field Inversion Method

Hocking et al.(2001) has proposed an inversion algorithm for determining the background mean wind field in the meteor ablation region based on the doppler technique, that can be described as follows:

Assuming that the background wind field is uniform for a certain time-height range and denoting $\boldsymbol{v} = (\overline{u}, \overline{v}, \overline{w})$, with $\overline{u}$, $\overline{v}$, and $\overline{w}$ being the mean wind field in the zonal, meridional, and vertical directions, respectively. The radial velocity $\overline{v}_{\rm rad}$ can be expressed as (Hocking et al., 2001):

$$\overline{v}_{\rm rad} = \boldsymbol{v}\cdot\boldsymbol{l} = \overline{u}\cos\theta_x + \overline{v}\cos\theta_y + \overline{w}\cos\theta_z, \tag{1}$$

where $\boldsymbol{l}$ is a unit vector along the radial direction (the direction of the observer's sightline), and θ_x, θ_y, and θ_z represent the angles of $\boldsymbol{l}$ with the east direction (x), the north direction (y), and the zenith direction (z), respectively. The zenith angle (θ) and azimuth angle (ϕ) at which the meteoroid is detected correspond to θ_x, θ_y, and θ_z in the following way (Hocking et al., 2001):

$$\begin{cases}\cos\theta_x = \sin\theta\cos\phi\\ \cos\theta_y = \sin\theta\sin\phi\\ \cos\theta_z = \cos\theta\end{cases}. \tag{2}$$

For any three radial velocities $v_{\rm rad1}$, $v_{\rm rad2}$, and $v_{\rm rad3}$ whose radial directions are not in the same plane, the mean wind field in the region can be obtained by solving a system of linear equations. Denote that the angles between $v_{{\rm rad}i}$ and the east, north, and zenith directions are θ_{xi}, θ_{yi}, and θ_{zi}, respectively. Then there is:

$$\begin{bmatrix}\overline{u}\\ \overline{v}\\ \overline{w}\end{bmatrix} = \begin{bmatrix}\cos\theta_{x1} & \cos\theta_{y1} & \cos\theta_{z1}\\ \cos\theta_{x2} & \cos\theta_{y2} & \cos\theta_{z2}\\ \cos\theta_{x3} & \cos\theta_{y3} & \cos\theta_{z3}\end{bmatrix}^{-1}\begin{bmatrix}v_{\rm rad1}\\ v_{\rm rad2}\\ v_{\rm rad3}\end{bmatrix}. \tag{3}$$

The presence of disturbances causes the background wind in the detection area to become not uniform. This results in an error between the velocity of the mean wind field projected in the radial direction and the actual radial velocity at that location. Denote the error between the velocity of the background mean wind field projected in the ith radial direction and the measured radial velocity at that location as ϵ_{vi}. By using the least squares method (Hocking et al., 2001):

$$\epsilon_v^2 = \sum_{i=1}^{m}\epsilon_{vi} = \sum_{i=1}^{m}\left(\overline{u}\cos\theta_{xi} + \overline{v}\cos\theta_{yi} + \overline{w}\cos\theta_{zi} - v_{{\rm rad}i}\right)^2, \tag{4}$$

where ϵ_v^2 is the error term and $\sum_{i=1}^{m}\epsilon_{vi}$ denotes the summation of the 1st to mth terms. To minimize ϵ_v^2, let the partial derivatives of Equation (4) with respect to $\overline{u}$, $\overline{v}$, and $\overline{w}$ be zero. The results are:

$$\begin{cases}\dfrac{\partial\epsilon_v^2}{\partial\overline{u}} = 2\sum_{i=1}^{m}\left(\overline{u}\cos\theta_{xi} + \overline{v}\cos\theta_{yi} + \overline{w}\cos\theta_{zi} - v_{{\rm rad}i}\right)\cdot\left(\sum_{i=1}^{m}\cos\theta_{xi}\right) = 0\\ \dfrac{\partial\epsilon_v^2}{\partial\overline{v}} = 2\sum_{i=1}^{m}\left(\overline{u}\cos\theta_{xi} + \overline{v}\cos\theta_{yi} + \overline{w}\cos\theta_{zi} - v_{{\rm rad}i}\right)\cdot\left(\sum_{i=1}^{m}\cos\theta_{yi}\right) = 0\\ \dfrac{\partial\epsilon_v^2}{\partial\overline{w}} = 2\sum_{i=1}^{m}\left(\overline{u}\cos\theta_{xi} + \overline{v}\cos\theta_{yi} + \overline{w}\cos\theta_{zi} - v_{{\rm rad}i}\right)\cdot\left(\sum_{i=1}^{m}\cos\theta_{zi}\right) = 0\end{cases}. \tag{5}$$

Thus,

$$\begin{bmatrix}\sum_{i=1}^{m}\cos\theta_x\cos\theta_x & \sum_{i=1}^{m}\cos\theta_y\cos\theta_x & \sum_{i=1}^{m}\cos\theta_z\cos\theta_x\\ \sum_{i=1}^{m}\cos\theta_x\cos\theta_y & \sum_{i=1}^{m}\cos\theta_y\cos\theta_y & \sum_{i=1}^{m}\cos\theta_z\cos\theta_y\\ \sum_{i=1}^{m}\cos\theta_x\cos\theta_z & \sum_{i=1}^{m}\cos\theta_y\cos\theta_z & \sum_{i=1}^{m}\cos\theta_z\cos\theta_z\end{bmatrix}\begin{bmatrix}\overline{u}\\ \overline{v}\\ \overline{w}\end{bmatrix} = \begin{bmatrix}\sum_{i=1}^{m}v_{{\rm rad}i}\cos\theta_x\\ \sum_{i=1}^{m}v_{{\rm rad}i}\cos\theta_y\\ \sum_{i=1}^{m}v_{{\rm rad}i}\cos\theta_z\end{bmatrix}. \tag{6}$$

The background mean wind field is obtained by substituting Equation (2) into Equation (6):

$$\begin{bmatrix} \overline{u} \\ \overline{v} \\ \overline{w} \end{bmatrix} = \begin{bmatrix} \sum_{i=1}^{m}\sin^2\theta_i\cos^2\phi_i & \sum_{i=1}^{m}\sin^2\theta_i\sin\phi_i\cos\phi_i & \sum_{i=1}^{m}\sin\theta_i\cos\theta_i\cos\phi_i \\ \sum_{i=1}^{m}\sin^2\theta_i\sin\phi_i\cos\phi_i & \sum_{i=1}^{m}\sin^2\theta_i\sin^2\phi_i & \sum_{i=1}^{m}\sin\theta_i\cos\theta_i\sin\phi_i \\ \sum_{i=1}^{m}\sin\theta_i\cos\theta_i\cos\phi_i & \sum_{i=1}^{m}\sin\theta_i\cos\theta_i\sin\phi_i & \sum_{i=1}^{m}\cos^2\theta_i \end{bmatrix}^{-1} \begin{bmatrix} \sum_{i=1}^{m}v_{\mathrm{rad}i}\sin\theta_i\cos\phi_i \\ \sum_{i=1}^{m}v_{\mathrm{rad}i}\sin\theta_i\sin\phi_i \\ \sum_{i=1}^{m}v_{\mathrm{rad}i}\cos\theta_i \end{bmatrix}. \tag{7}$$

In Equations (1) to (7), the east direction is the starting point of the azimuth angle, and the anti-clockwise direction is the positive direction, while the azimuth angle recorded by the Meridian Project meteor radar is the northward direction as the starting point of the azimuth angle, and the clockwise direction is the positive direction. Therefore, the azimuth angle needs to be preprocessed before data inversion.

2.2 Gravity Wave Disturbances Variance and Gravity Wave Momentum Fluxes Inversion Method

The inversion algorithm based on the least squares fitting algorithm to solve for a certain range of disturbance variance and gravity wave momentum fluxes is as follows (Hocking, 2005): The measured radial velocity at a given place can be expressed as the mean radial velocity plus the disturbed radial velocity at that site:

$$v_{\mathrm{rad}} = \overline{v}_{\mathrm{rad}} + v'_{\mathrm{rad}}. \tag{8}$$

The variable v'_{rad} reflects the high-frequency fluctuations after removing the effects of background winds, planetary waves, and tidal waves. It can be used to calculate the gravity wave disturbances variance and the gravity wave momentum fluxes.

Let u', v', and w' represent the mean perturbations of the zonal, meridional, and vertical winds. Then the mean perturbation projection in the radial direction $v'_{\mathrm{rad}m}$ can be written as:

$$v'_{\mathrm{rad}m} = u'\sin\theta\cos\phi + v'\sin\theta\sin\phi + w'\cos\theta. \tag{9}$$

The sum of the mean square deviation of v'_{rad} and $v'_{\mathrm{rad}m}$ in the radial direction can be expressed as:

$$\begin{aligned} \Lambda &= \sum_{i=1}^{m}\left[\left(v'_{\mathrm{rad}i}\right)^2 - \left(v'_{\mathrm{rad}m}\right)^2\right]^2 \\ &= \sum_{i=1}^{m}\left[\left(v'_{\mathrm{rad}i}\right)^2 - \left(u'\sin\theta_i\cos\phi_i + v'\sin\theta_i\sin\phi_i + w'\cos\theta_i\right)^2\right]^2 \\ &= \sum_{i=1}^{m}\left[\left(v'_{\mathrm{rad}}\right)^2 - \left(u'^2\sin^2\theta_i\cos^2\phi_i + v'^2\sin^2\theta_i\sin^2\phi_i + w'^2\cos^2\theta_i\right.\right. \\ &\quad + 2u'v'\sin^2\theta_i\sin\phi_i\cos\phi_i + 2u'w'\sin\theta_i\cos\theta_i\cos\phi_i \\ &\quad \left.\left. + 2v'w'\sin\theta_i\cos\theta_i\sin\phi_i\right)\right]^2, \end{aligned} \tag{10}$$

where $v'_{\mathrm{rad}i}$ represents the ith detected radial velocity, θ_i and ϕ_i are the corresponding zenith angle and azimuth angle, u'^2 and v'^2 represent the gravity wave disturbances variance induced by gravity waves in the zonal and meridional directions, respectively. And $u'w'$ and $v'w'$ are the zonal gravity wave momentum flux and meridional gravity wave momentum flux.

When Λ is taken to its minimum, that is, when the partial derivatives of Equation (10) with regard to u'^2, v'^2, w'^2, $u'v'$, $u'w'$, and $v'w'$ are zero, u', v', and w' are the closest to the real perturbations. Consequently,

$$\begin{bmatrix} \sum_{i=1}^{m}\sin^4\theta_i\cos^4\phi_i & \sum_{i=1}^{m}\sin^4\theta_i\sin^2\phi_i\cos^2\phi_i & \sum_{i=1}^{m}\sin^2\theta_i\cos^2\theta_i\cos^2\phi_i \\ \sum_{i=1}^{m}\sin^4\theta_i\sin^2\phi_i\cos^2\phi_i & \sum_{i=1}^{m}\sin^4\theta_i\sin^4\phi_i & \sum_{i=1}^{m}\sin^2\theta_i\cos^2\theta_i\sin^2\phi_i \\ \sum_{i=1}^{m}\sin^2\theta_i\cos^2\theta_i\cos^2\phi_i & \sum_{i=1}^{m}\sin^2\theta_i\cos^2\theta_i\sin^2\phi_i & \sum_{i=1}^{m}\cos^4\theta_i \\ \sum_{i=1}^{m}\sin^4\theta_i\sin\phi_i\cos^3\phi_i & \sum_{i=1}^{m}\sin^4\theta_i\sin^3\phi_i\cos\phi_i & \sum_{i=1}^{m}\sin^2\theta_i\cos^2\theta_i\sin\phi_i\cos\phi_i \\ \sum_{i=1}^{m}\sin^3\theta_i\cos\theta_i\cos^3\phi_i & \sum_{i=1}^{m}\sin^3\theta_i\cos\theta_i\sin^2\phi_i\cos\phi_i & \sum_{i=1}^{m}\sin\theta_i\cos^3\theta_i\cos\phi_i \\ \sum_{i=1}^{m}\sin^3\theta_i\cos\theta_i\sin\phi_i\cos^2\phi_i & \sum_{i=1}^{m}\sin^3\theta_i\cos\theta_i\sin^3\phi_i & \sum_{i=1}^{m}\sin\theta_i\cos^3\theta_i\cos\phi_i \end{bmatrix}$$

$$\begin{bmatrix} \sum_{i=1}^{m}2\sin^4\theta_i\sin\phi_i\cos^3\phi_i & \sum_{i=1}^{m}2\sin^3\theta_i\cos\theta_i\cos^3\phi_i & \sum_{i=1}^{m}2\sin^3\theta_i\cos\theta_i\sin\phi_i\cos^2\phi_i \\ \sum_{i=1}^{m}2\sin^4\theta_i\sin^3\phi_i\cos\phi_i & \sum_{i=1}^{m}2\sin^3\theta_i\cos\theta_i\sin^2\phi_i\cos\phi_i & \sum_{i=1}^{m}2\sin^3\theta_i\cos\theta_i\sin^3\phi_i \\ \sum_{i=1}^{m}2\sin^2\theta_i\cos^2\theta_i\sin\phi_i\cos\phi_i & \sum_{i=1}^{m}2\sin\theta_i\cos^3\theta_i\cos\phi_i & \sum_{i=1}^{m}2\sin\theta_i\cos^3\theta_i\sin\phi_i \\ \sum_{i=1}^{m}2\sin^4\theta_i\sin^2\phi_i\cos^2\phi_i & \sum_{i=1}^{m}2\sin^3\theta_i\cos\theta_i\sin\phi_i\cos^2\phi_i & \sum_{i=1}^{m}2\sin^3\theta_i\cos\theta_i\sin^2\phi_i\cos\phi_i \\ \sum_{i=1}^{m}2\sin^3\theta_i\cos\theta_i\sin\phi_i\cos^2\phi_i & \sum_{i=1}^{m}2\sin^2\theta_i\cos^2\theta_i\cos^2\phi_i & \sum_{i=1}^{m}2\sin^2\theta_i\cos^2\theta_i\sin\phi_i\cos\phi_i \\ \sum_{i=1}^{m}2\sin^3\theta_i\cos\theta_i\sin^2\phi_i\cos\phi_i & \sum_{i=1}^{m}2\sin^2\theta_i\cos^2\theta_i\sin\phi_i\cos\phi_i & \sum_{i=1}^{m}2\sin^2\theta_i\cos^2\theta_i\sin^2\phi_i \end{bmatrix} \begin{bmatrix} u'^2 \\ v'^2 \\ w'^2 \\ u'v' \\ u'w' \\ v'w' \end{bmatrix}$$

$$= \begin{bmatrix} \sum_{i=1}^{m}\sin^2\theta_i\cos^2\phi_i\left(v'_{\mathrm{rad}i}\right)^2 \\ \sum_{i=1}^{m}\sin^2\theta_i\sin^2\phi_i\left(v'_{\mathrm{rad}i}\right)^2 \\ \sum_{i=1}^{m}\cos^2\theta_i\left(v'_{\mathrm{rad}i}\right)^2 \\ \sum_{i=1}^{m}\sin^2\theta_i\sin\phi_i\cos\phi_i\left(v'_{\mathrm{rad}i}\right)^2 \\ \sum_{i=1}^{m}\sin\theta_i\cos\theta_i\cos\phi_i\left(v'_{\mathrm{rad}i}\right)^2 \\ \sum_{i=1}^{m}\sin\theta_i\cos\theta_i\sin\phi_i\left(v'_{\mathrm{rad}i}\right)^2 \end{bmatrix}. \tag{11}$$

3. Results

3.1 Meteor Count Statistics

In this study, the horizontal wind fields, gravity wave disturbances variance, and gravity wave momentum fluxes are inverted using the 2012–2022 data from the Meridian Project meteor radar at the Mohe station in Heilongjiang and the Zuoling station in Wuhan. The results of daily meteor counts for 2012–2022 at Mohe and Zuoling are shown and summarized below:

The number of meteors detected at the Mohe station and Zuoling station between 2012 and 2022 is depicted in Figure 1. At Mohe station, there are between 15,000 and 35,000 meteors recorded every day, with a distinct yearly variation pattern indicating more meteors in June through November and fewer in December through May (Figure 1a). Between 2012 and 2017, Zuoling station recorded much fewer meteors than Mohe station. In 2018, the total number of meteors increased, although it was still fewer than the counts at Mohe station. Starting from 2018, the quantity of meteoroids observed at the Zuoling station is almost the same as that at the Mohe station during the months of November to December and January to April. However, there is a modest fall in the number of meteors from May to July, followed by a gradual increase. This study primarily focuses on inverting the horizontal wind fields, gravity wave disturbances variance, and gravity wave momentum fluxes in the region where the meteor radar at both Mohe and Zuoling stations find strong echo signals at the 79–97 km region.

3.2 Inversion of Horizontal Wind Fields, Gravity Wave Disturbances Variance and Gravity Wave Momentum Fluxes

In order to guarantee the validity of the results, at least 30 data points of meteor radar observations are required to complete the calculation of the gravity wave momentum fluxes (Fritts et al., 2012a, b). Therefore, the inversion is done by the Composite Day method, which means all meteors detected in a natural month are considered as a single data point (Andrioli et al., 2013, Liu AZ et al., 2013). To eliminate the effects of tidal and planetary waves, a sliding window with a time length of 2 hours and a height of 3 kilometers is used, and the corresponding time-height sliding steps are 1 hour and 3 kilometers, respectively. The inversion result of each window represents the value of the parameter at the center of the corresponding time-height window (Hocking, 2005).

For each window, to avoid the measurement errors caused by excessively large or small zenith angles, only meteors with zenith angles ranging from 15° to 60° were considered (Jia MJ et al., 2018). Additionally, meteors with rapid speed decay and radial velocities above 200 m/s were excluded. According to Vincent et al. (2010), a minimum of 6–10 meteors per time window is needed to accurately inverse a horizontal wind field for one data point. Andrioli et al. (2013) suggest that at least 30 meteors per time height window should be used when employing the Composite Day method. To determine the mean background wind field, the zenith angles, azimuths, and radial velocities of all meteors detected in the window should be substituted into Equation (7). The data is then checked to ensure that the absolute value of the disturbed radial velocity was less than 25 m/s, i.e.,

$$|v'_{\rm rad}| = |v_{\rm rad} - \overline{v}_{\rm rad}| = \left|v_{\rm rad} - \overline{u}\sin\theta\cos\phi - \overline{v}\sin\theta\sin\phi\right| < 25. \quad (12)$$

The zenith angle, azimuth angle, and radial velocity data of meteors that meet the screening conditions are reintroduced into Equation (7) to calculate the mean background wind field. Again, use Equation (12) for screening. Repeat the above process until all the

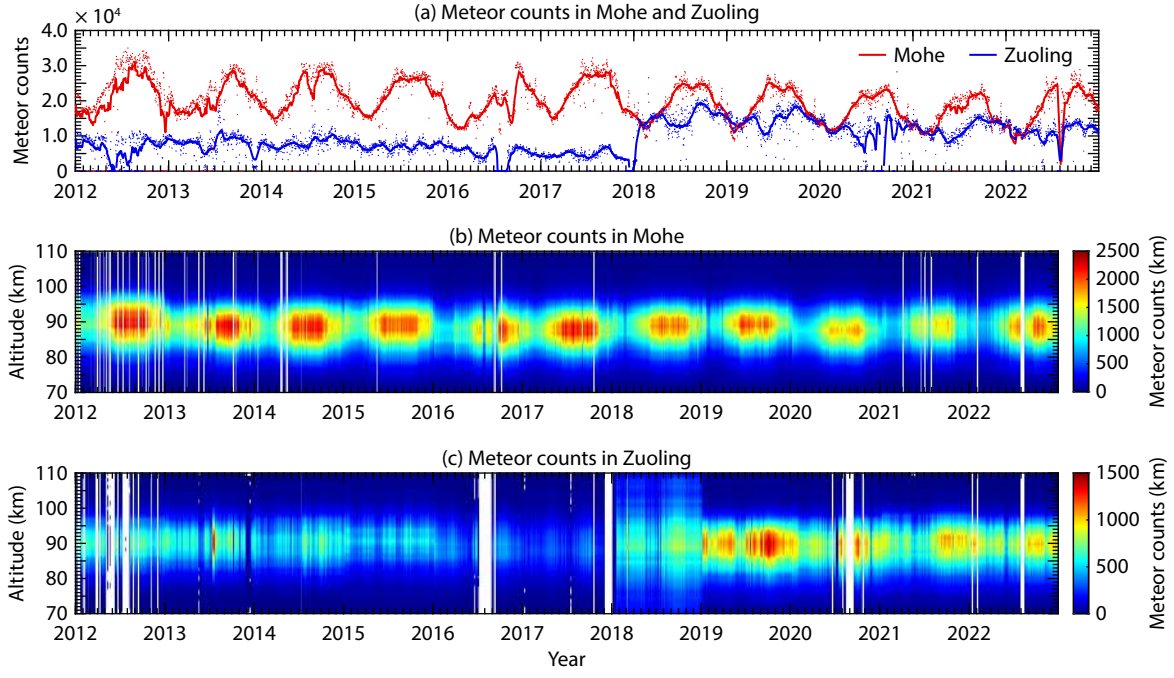

Figure 1. (a) Daily meteor counts; dots are daily meteor counts; and solid line is 30-day sliding mean curves of meteor counts, with Mohe station in red and Zuoling station in blue; (b) Height contour plot of meteor counts at Mohe station; and (c) Height contour plot of meteor counts at Zuoling station.

retained data is calculated to satisfy Equation (12). The wind field error obtained at this time is the smallest, which can represent the actual wind field at this position (Holdsworth et al., 2004).

This study presents all deduced observations from 2012 to 2022 at Mohe and Zuoling stations. The horizontal wind field of 77.5–98.5 km and the gravity wave disturbances variance and gravity wave momentum fluxes of 79–97 km were inverted. The inversion results are averaged month by month to obtain the horizontal wind fields, gravity wave disturbances variance, and gravity wave momentum fluxes variations at the two stations, are all shown in Figures 2–7.

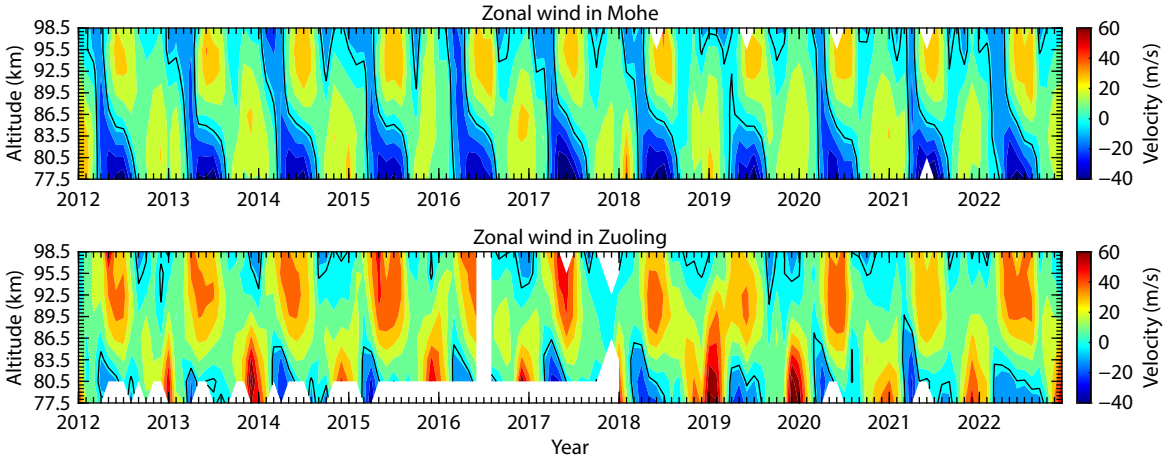

Figure 2. Zonal wind fields at Mohe and Zuoling stations, 2012–2022. The solid black line represents the 0 m/s contour.

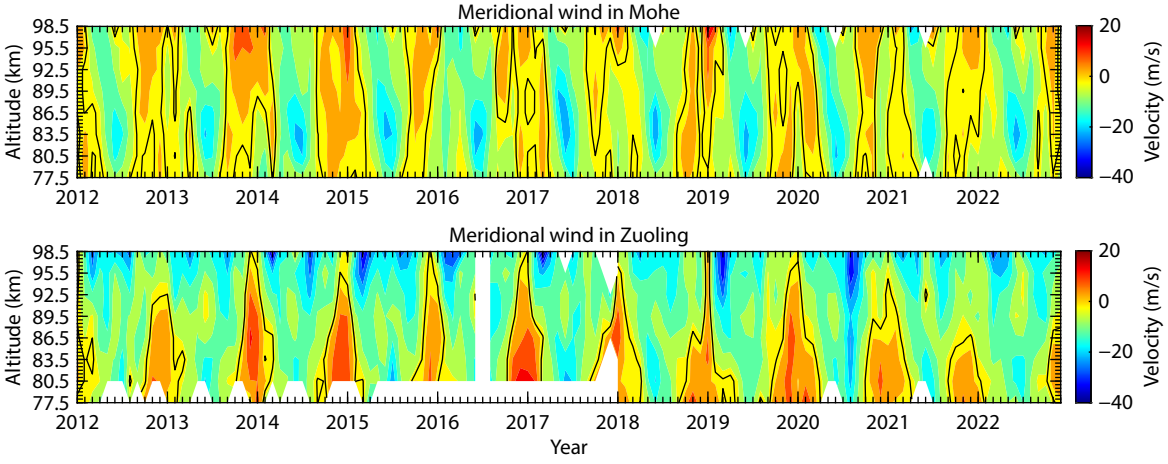

Figure 3. Meridional wind fields at Mohe and Zuoling stations, 2012–2022. The solid black line represents the 0 m/s contour.

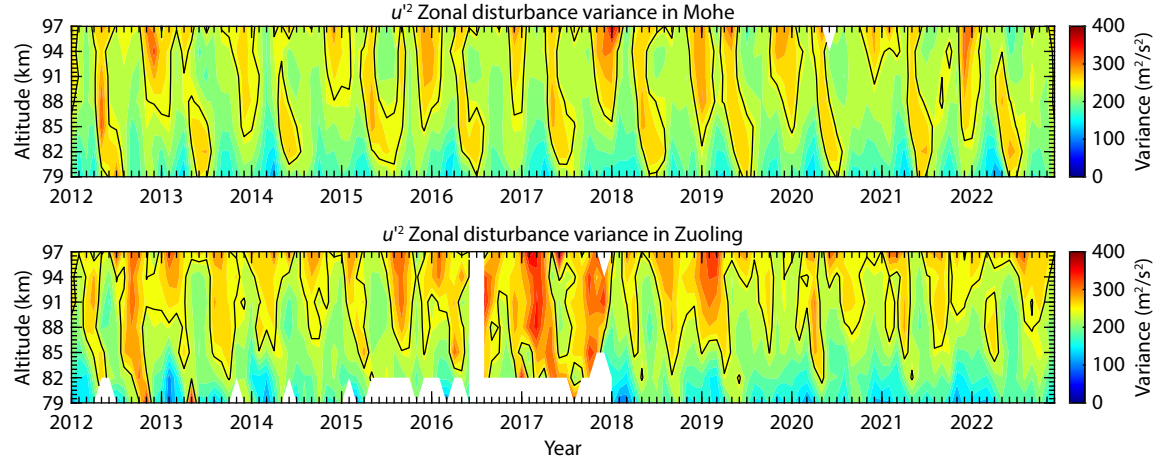

Figure 4. Zonal GW disturbances variance at Mohe and Zuoling stations, 2012–2022. The solid black line represents the 250 m^2/s^2 contour.

The zonal wind at Mohe station and Zuoling station has an obvious annual variation characteristics (see Figure 2). The zonal wind above 85 km at Mohe station is mainly eastward. At 77.5–83.5 km, it is westward from March to August every year. At 92.5–98.5 km, January–March and September–October are westward. Westward wind prevails at Zuoling Station between 77.5 and 86.5 km from March to June each year. Zonal wind at 86.5 to 92.5 km is predominantly eastward throughout the year, with westward wind only occurring in March of 2020 and 2021. Westward wind is observed at 92.5 to 98.5 km from September to October or September to

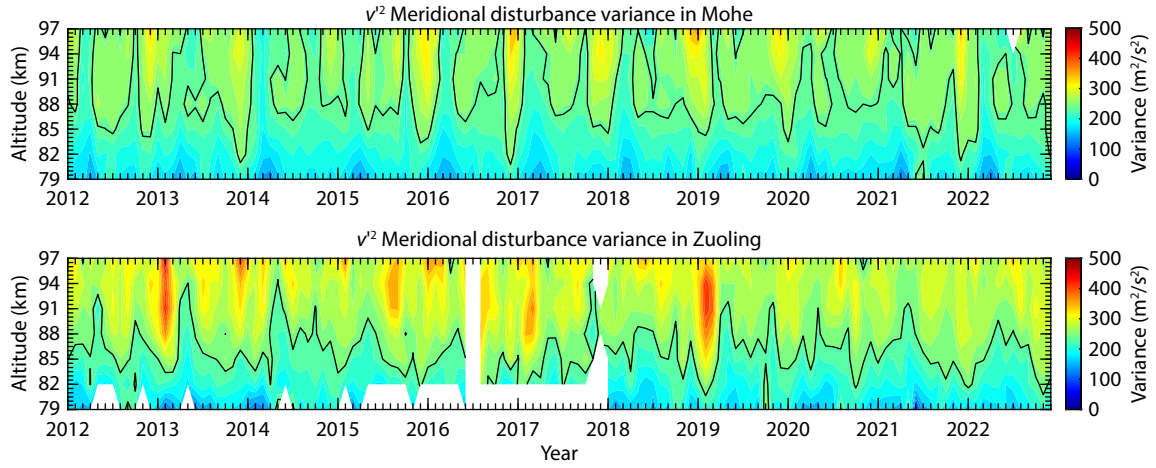

Figure 5. Meridional GW disturbances variance at Mohe and Zuoling stations, 2012–2022. The solid black line represents the 250 m^2/s^2 contour.

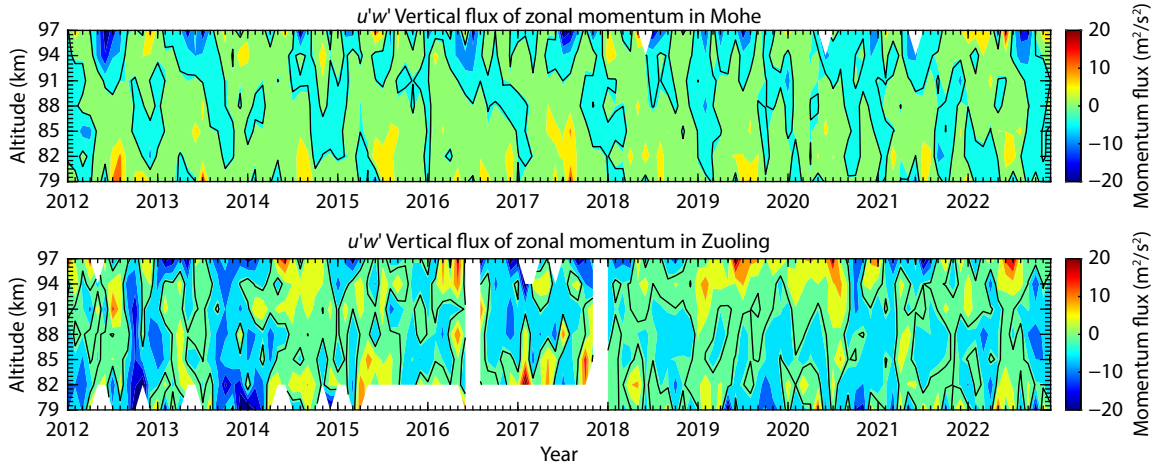

Figure 6. The zonal GW momentum fluxes at Mohe and Zuoling stations, 2012–2022. The solid black line represents the 0 m^2/s^2 contour.

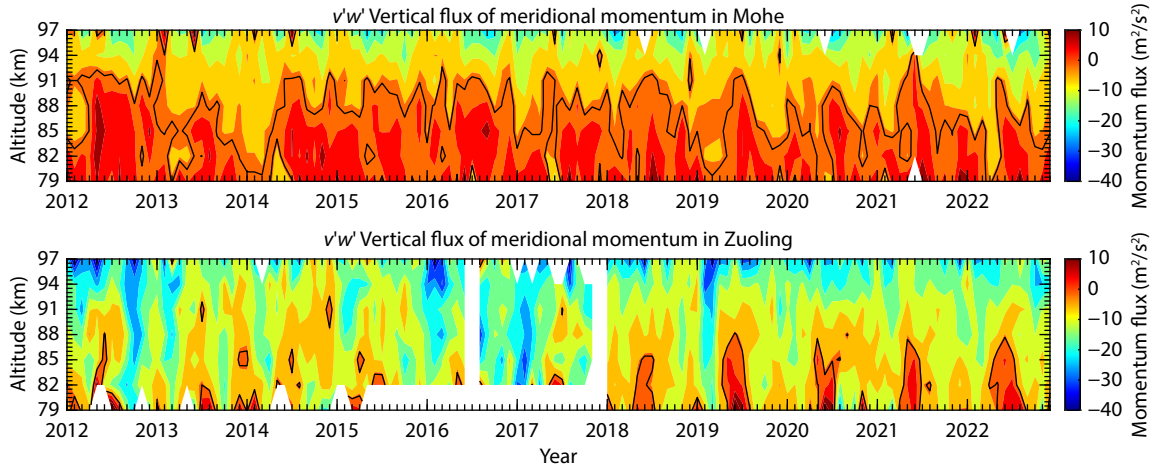

Figure 7. The meridional GW momentum fluxes at Mohe and Zuoling stations, 2012–2022. The solid black line represents the 0 m^2/s^2 contour.

December annually.

The meridional winds in Mohe and Zuoling also exhibit a distinct annual variation pattern (see Figure 3). The meridional winds are dominated by the south wind from March to August every year, while northward winds occur only from September to December and from January to March. Whereas, there are still some differences in the distribution of meridional winds between the two regions. The meridional wind near the Zuoling station gradually reversed from northward to southward as altitude increased. The variation in the meridional wind with height near Mohe Station is not as pronounced as that near Zuoling Station.

There is an annual variation in the zonal GW disturbances variance of Mohe station and Zuoling station: the disturbances variance of the two stations in October–December and April–July are significantly greater than that in other months (see Figure 4). The zonal disturbance variance of Mohe station has a maximum value from November to December every year. From May to July, the disturbance variance near 85 km suddenly decreases, which is speculated to be related to gravity wave breaking. The zonal disturbance variance of Zuoling station has a maximum value in April and October every year. The disturbance variance gradually increases with the increase in height, but the variation in disturbance variance from June to July 2017 does not conform to this law but decreases first and then increases with the height, forming a 'hole' in the contour map.

The meridional GW disturbance variance at Mohe station reaches its maximum value in November and December (see Figure 5). The meridional disturbance variance in the height range of 88–95 km suddenly decreases from March to July, and meridional disturbances variance in the remaining months increase steadily with the increase in height. The meridional disturbance variance of Zuoling station increases gradually with the increase in height, and the maximum value appears in January–February and September–October every year. However, the 250 m^2/s^2 contour exhibits an obvious upward trend from April to July every year.

The annual variation pattern of the zonal gravity wave momentum flux at Mohe Station is not evident (see Figure 6). With increasing altitude, the zonal gravity wave momentum flux exhibits an overall trend from eastward to gradually westward. The maximum westward momentum flux appears in July–August each year at around 97 km, while the maximum eastward momentum flux appears in August–September each year at around 79 km. The zonal momentum flux at Zuoling Station is mainly westward in 2012–2014, 2016–2018, and August 2021–2022 as a whole, with the maximum value occurring in August–October, near 79 km. 2014–2016 and 2018–August 2021 are dominated by eastward momentum flux overall, with the maximum value occurring in May–July, near 97 km.

The meridional momentum flux at the Mohe station increases with height as a whole, and shifts from northward to southward as altitude increases (see Figure 7). The zero-value line drops to about 85 km from December to March of the next year. In 2014, 2019, and 2022, both the altitude and temporal characteristics of this variation become more significant. The meridional momentum flux at Zuoling Station increases as a whole and changes from northward to southward with increasing altitude. The maximum value of the northward momentum flux appears every year in May–July at an altitude around 79 km, while the maximum value of the southward momentum flux appears every year in February–April at an altitude around 97 km.

Comparing the variations between gravity wave momentum fluxes (see Figures 6 and 7) and the horizontal wind fields (see Figures 2 and 3), it has been observed that when the momentum flux reaches its peak, the wind field also reaches its maximum value, and the direction of the momentum flux is opposite to the direction of the horizontal wind field. The relationship between gravity wave momentum fluxes and the horizontal wind fields is further elaborated below.

The westward GW momentum flux at the Mohe station is at its maximum at 97 km in June 2012, July 2017, and July 2022. The eastward momentum flux reaches its maximum at 79 km in August 2012, July 2013, August 2017, and August 2019. During these periods, the wind field direction is opposite to the momentum flux direction. The remaining years also have similar characteristics. At the Mohe station in January 2012, May 2012, June 2016, and January 2022, the northward maximum of the gravity wave momentum flux appears near 79 km, while the meridional wind field is southward. The eastward momentum flux at the Zuoling station reaches a maximum of around 97 km in January 2012 and June 2019, while the zonal wind field is westward. The westward momentum flux reaches a maximum around 82 km in October 2012 and November 2013, corresponding to an eastward zonal wind field, which is the maximum wind field for that time period. The maximum of southward momentum flux appears at about 79 km, in June 2019 and May 2020, which corresponds to a northward meridional wind field.

The observations in this study are consistent with the gravity wave filtering theory originally proposed by Lindzen (1981). According to this theory, when the background wind is westward, the westward gravity waves are filtered by the westward background wind. Only the eastward gravity waves continue to propagate. After the eastward gravity wave reach the critical point and breakup, it will deposit its momentum into the background atmosphere, and drag the background wind to the east, so that the eastward gravity wave is filtered and the westward gravity wave is uploaded. The specific performance in this study is as follows: the gravity wave momentum flux of Mohe station and Zuoling station is affected by the background wind filtering effect, and the gravity wave in the same direction as the wind field is suppressed, so that the gravity wave momentum flux is opposite to the direction of the wind field. The horizontal wind field is affected by the gravity wave breaking and turns in the same direction as before the gravity wave breaking, so that the same direction gravity wave is filtered. When the gravity wave momentum flux reaches the maximum value, the horizontal wind field also reaches the maximum value, and the two directions are opposite.

In addition, upon comparing the observations from the two stations, it is evident that the absolute values of the horizontal wind fields, gravity wave disturbances variance, and gravity wave momentum fluxes at Mohe Station are generally smaller than

those at Zuoling Station. This indicates that the atmospheric activity in the Mesosphere and Lower Thermosphere (MLT) region at Mohe Station is weaker than that at Zuoling Station.

3.3 Lomb–Scargle Power Spectrum Analysis

In order to investigate the periodic characteristics of the wind fields and gravity wave activity in the MLT region, this study also conducted a Lomb–Scargle periodogram analysis of the horizontal wind fields, gravity wave disturbances variance, and gravity wave momentum fluxes at Mohe and Zuoling stations from 2012 to 2022.

Figure 8 indicates the power spectrum densities of the periodic characteristics of each parameter at the Mohe and Wuhan stations. Two kinds of zonal winds, with periods of 12 and 6 months, are observed at both stations. At the Mohe station, zonal wind with a period of 6 months mainly appears above 89.5 km, whereas at the Zuoling station, zonal wind with a 6-month period mainly appears below 86.5 km. There are three types of zonal gravity wave disturbances variance, with periods of 4, 6, and 12 months at both stations. Among these, the 4-month zonal disturbance variance at Mohe Station is mainly distributed above 85 km, while the 4-month zonal disturbance variance at Zuoling Station is mainly distributed below 85 km. The distribution height of the 6-month period zonal gravity wave disturbance variance at Mohe Station (79–86 km) is lower than that at Zuoling Station (85–92 km). The 12-month zonal disturbance variance at Mohe Station is mainly distributed above 94 km and below 85 km, whereas it is only noticeable below 84 km at Zuoling Station.

The meridional winds at both Mohe and Zuoling stations exhibit clear 12-month period and 6-month period (Figure 9). Among them, the distribution height of meridional winds with a 6-month period at Mohe Station (78–87 km) is lower than that at Zuoling Station (85–98.5 km). At the Mohe station, the meridional gravity wave disturbance variance with a 12-month period occurs above 91 km and below 85 km, the meridional disturbance variance with a period of 6 months occurs at all heights, and the meridional disturbance variance with a period of 4 months appears only above 90 km. At the Zuoling station, the meridional gravity wave disturbance variance with a 12-month period appears below 94 km and above 96 km, while the meridional disturbance variance

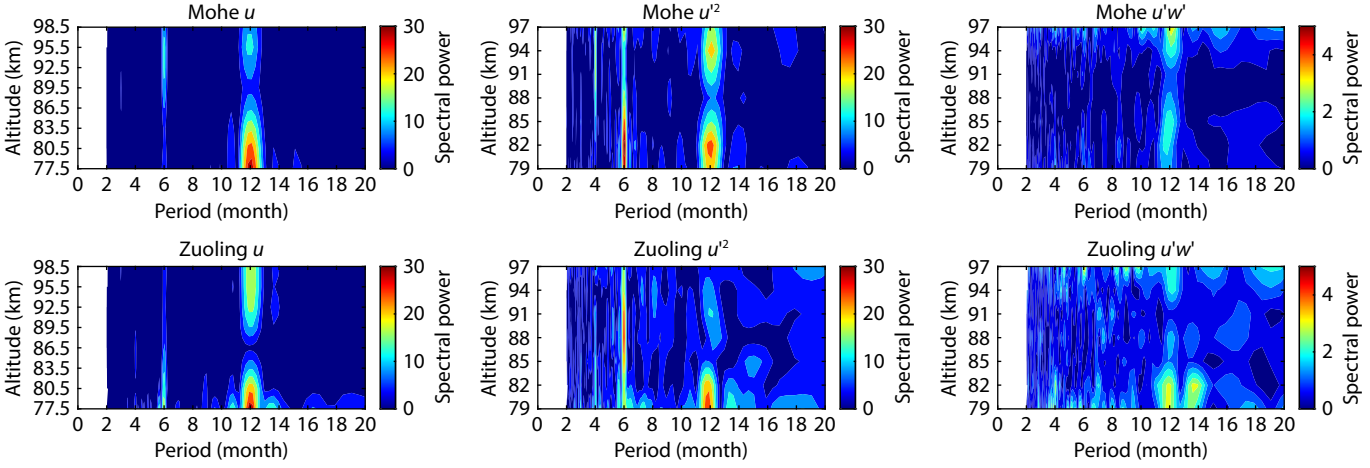

Figure 8. Lomb–Scargle power spectral analysis of zonal wind fields, zonal gravity wave disturbances variance, and zonal gravity wave momentum fluxes at Mohe and Zuoling stations, 2012–2022.

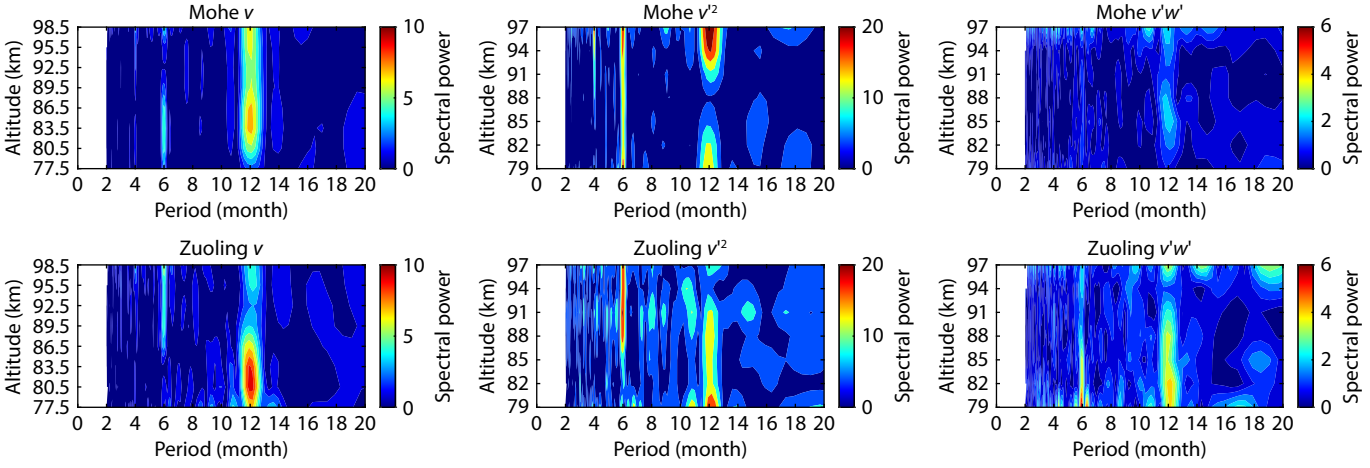

Figure 9. Lomb–Scargle power spectral analysis of the meridional wind fields, meridional gravity wave disturbances variance, and meridional gravity wave momentum fluxes at Mohe and Zuoling stations, 2012–2022.

with a 6-month period appears above 86 km.

The meridional gravity wave momentum flux with a 12-month period at Mohe station is distributed in the range of 82–91 km and 94–97 km, while the meridional momentum flux with a 12-month period at Zuoling station is distributed in the range of higher than 96 km and lower than 93 km. The meridional momentum flux with a 6-month is mainly found in the range of lower than 88 km.

Comparison of Figure 8 and Figure 9 reveals that the power spectral density of the zonal wind field is approximately 3.5 times that of the meridional wind field. The power spectral density of the zonal gravity wave disturbance variance is about 1.5 times that of the meridional gravity wave disturbance variance. Additionally, the power spectral density of the gravity wave momentum flux in the zonal direction is comparable to that in the meridional direction. With increasing altitude, the power spectral densities of the meridional and zonal parameters (wind fields, gravity wave disturbances variance, and gravity wave momentum fluxes) for 12-month and 6-month periods at both stations indicate intermittent patterns in the vertical direction, with peaks typically observed at two distinct altitude/height zones; i.e., below 88 km and above 94 km.

4. Conclusions

In this paper, the horizontal wind field, GW disturbance variance and momentum flux in Mohe and Zuoling stations of the Chinese Meridian Project are inverted by using the observational data of meteor radar from 2012 to 2022. The results show that the zonal wind at Mohe station has obvious annual variation pattern. The zonal wind above 85 km is mainly eastward, but around 77.5–83.5 km westward wind appears from March to August every year, and around 92.5–98.5 km westward wind manifests from January to March and September to October every year. The meridional wind is southward from March to August every year. As the height increases, the southward wind gradually increases. The zonal wind at Zuoling station is mainly eastward above 85 km, westward from March to June at around the altitutde of 77.5–86.5 km every year, eastward around 86.5–92.5 km heights almost all year round, and westward from September to October or September to December at around 92.5–98.5 km every year. The meridional wind is mainly southward, and only northward winds appear in September–December and January–March each year. The northward wind will gradually decrease with height, and eventually reverse to the southward wind.

The zonal and meridional GW disturbance variances of Mohe station and Zuoling station gradually increase with the increase of height, and may suddenly decrease at 85–95 km due to gravity wave breaking, and then continue to increase again thereafter. At Mohe station and Zuoling station, only the meridional gravity wave fluctuation flux increases with height, gradually changing from northward to southward, and no obvious change in the rule or law is found in the zonal momentum flux. The horizontal wind field, disturbance variance and gravity wave fluctuation flux at Mohe station are generally smaller than those at Zuoling station, indicating that the semidiurnal tides over Mohe should be stronger than Zuoling.

According to the results of Lomb–Scargle periodogram analysis, the horizontal wind field, disturbance variance and gravity fluctuation flux of Mohe station and Zuoling station have obvious 12-month period and 6-month period. The power spectral density of zonal and meridional horizontal wind field, disturbance variance and momentum flux at Mohe station and Zuoling station is different, but the variation characteristics with height are similar. With the increase of height, the power spectral density of 12 months and 6 months at Mohe station and Zuoling station increases–decreases–increases again. The disturbance variance of horizontal wind field and gravity wave generally has only 12-month and 6-month periods, and the disturbance variance also has a more obvious 4-month period. The power spectral density of horizontal wind field, disturbance variance and gravity fluctuation flux at Mohe station and Zuoling station usually has a maximum value below 88 km and above 94 km, and other heights are small.

Acknowledgments

This work is supported by the Fundamental Research Funds for the Central Universities, CHD (NO. 300102263205 and NO. 300102264916), and the West Light Cross-Disciplinary Innovation team of Chinese Academy of Sciences (NO. E1294301). We acknowledge the Chinese Meridian Project for the ground-based observational data of the ionospheric plasma drift.

References

Andrioli, V. F., Fritts, D. C., Batista, P. P., and Clemesha, B. R. (2013). Improved analysis of all-sky meteor radar measurements of gravity wave variances and momentum fluxes. *Ann. Geophys.*, *31*(5), 889–908. https://doi.org/10.5194/angeo-31-889-2013

Chen, J. S., Xu, L. L., Ma, C. B., Li, N., and Lin, L. K. (2016). A new method of determining momentum flux based on the all-sky meteor radar. *Chin. J. Radio Sci. (in Chinese)*, *31*(6), 1124–1131. https://doi.org/10.13443/j.cjors.2015123002

Fang, X., Gu, S. Y., Ban, C., Li, T., Xiong, J. G., Ning, B. Q., Dou, X. K., and Wang, N. N. (2013). Horizontal wind comparison between sodium temperature/wind lidar over Hefei and meteor radar over Wuhan. *Chin. J. Quant. Electron. (in Chinese)*, *30*(1), 12–16. https://doi.org/10.3969/j.issn.1007-5461.2013.01.003

Fritts, D. C., Janches, D., Hocking, W. K., Mitchell, N. J., and Taylor, M. J. (2012a). Assessment of gravity wave momentum flux measurement capabilities by meteor radars having different transmitter power and antenna configurations. *J. Geophys. Res.: Atmos.*, *117*(D10), D10108. https://doi.org/10.1029/2011JD017174

Fritts, D. C., Janches, D., Iimura, H., Hocking, W. K., Bageston, J. V., and Leme, N. M. P. (2012b). Drake Antarctic Agile Meteor Radar first results: Configuration and comparison of mean and tidal wind and gravity wave momentum flux measurements with Southern Argentina Agile Meteor Radar. *J. Geophys. Res.: Atmos.*, *117*(D2), D02105. https://doi.org/10.1029/2011JD016651

Gu, S. Y., Li, T., Liu, A., Swenson, G., Gardner, C., Riggin, D., and Fritts, D. (2013). Comparison of the simultaneous horizontal wind observations by Na lidar, meteor radar and medium frequency radar. *Chin. J. Quant. Electron. (in Chinese)*, *30*(1), 7–11. https://doi.org/10.3969/j.issn.1007-5461.2013.02.007

Hao, X. J., Wang, L. B., Ma, Y., Wang, X. B., Yi, W., Ding, Z. H., and Li, N. (2023). Comparative analysis of horizontal wind observation in 70~100 km near space by meteor radar and medium frequency radar. *Aerosp. Technol. (in Chinese)*, (1), 43–52. https://doi.org/10.16338/j.issn.2097-0714.20220189

Hocking, W. K., Fuller, B., and Vandepeer, B. (2001). Real-time determination of meteor-related parameters utilizing modern digital technology. *J. Atmos. Sol. Terr. Phys.*, *63*(2-3), 155–169. https://doi.org/10.1016/S1364-6826(00)00138-3

Hocking, W. K. (2005). A new approach to momentum flux determinations using SKiYMET meteor radars. *Ann. Geophys.*, *23*(7), 2433–2439. https://doi.

org/10.5194/angeo-23-2433-2005

Holdsworth, D. A., Reid, I. M., and Cervera, M. A. (2004). Buckland Park all-sky interferometric meteor radar. *Radio Sci.*, *39*(5), RS5009. https://doi.org/10.1029/2003rs003014

Horne, J. H., and Baliunas, S. L. (1986). A prescription for period analysis of unevenly sampled time series. *Astrophys. J.*, *302*, 757–763. https://doi.org/10.1086/164037

Jia, M. J., Xue, X. H., Gu, S. Y., Chen, T. D., Ning, B. Q., Wu, J. F., Zeng, X. Y., and Dou, X. K. (2018). Multiyear observations of gravity wave momentum fluxes in the midlatitude mesosphere and lower thermosphere region by meteor radar. *J. Geophys. Res.: Space Phys.*, *123*(7), 5684–5703. https://doi.org/10.1029/2018JA025285

Jiang, G. Y., Xiong, J. G., Wan, W. X., Ning, B. Q., and Liu, L. B. (2005). The quasi 16-day waves in the mesosphere and lower thermosphere at Wuhan. *Chin. J. Space Sci. (in Chinese)*, *25*(1), 44–51. https://doi.org/10.11728/cjss2005.01.044

Liu, A. Z., Lu, X., and Franke, S. J. (2013). Diurnal variation of gravity wave momentum flux and its forcing on the diurnal tide. *J. Geophys. Res.: Atmos.*, *118*(4), 1668–1678. https://doi.org/10.1029/2012JD018653

Lomb, N. R. (1976). Least-squares frequency analysis of unequally spaced data. *Astrophys. Space Sci.*, *39*(2), 447–462. https://doi.org/10.1007/BF00648343

Scargle, J. D. (1982). Studies in astronomical time series analysis. II-Statistical aspects of spectral analysis of unevenly spaced data. *Astrophys. J.*, *263*, 835–853. https://doi.org/10.1086/160554

Vincent, R. A., Kovalam, S., Reid, I. M., and Younger, J. P. (2010). Gravity wave flux retrievals using meteor radars. *Geophys. Res. Lett.*, *37*(14), L14802. https://doi.org/10.1029/2010GL044086

Xiong, J. G., Wan, W. X., Ning, B. Q., and Liu, L. B. (2003). Tides in the mesosphere and lower thermosphere over Wuhan revealed by a meteor radar. *Chin. J. Space Sci. (in Chinese)*, *23*(5), 361–370. https://doi.org/10.3969/j.issn.0254-6124.2003.05.006

Yang, J. F., Xiao, C. Y., Hu, X., and Xu, Q. C. (2017). Observations and simulations of the mean winds in mesosphere and lower thermosphere over Langfang of China. *Chin. J. Space Sci. (in Chinese)*, *37*(3), 284–290. https://doi.org/10.11728/cjss2017.03.284

Yi, W., Xue, X. H., Zeng, J., Wang, J. Y., Zhou, B. Z., Ye, H. L., Chen, T. D., and Dou, X. K. (2023). Observation of MLT region winds and tides by the USTC Mengcheng meteor radar. *J. Univ. Sci. Technol. China*, *53*(5), 0501. https://doi.org/10.52396/JUSTC-2022-0158

Zhang, R. J., Gong, W. L., and Zhou, X. M. (2022). Research on atmospheric wind field in MLT region based on Beijing meteor radar. *J. Terahertz Sci. Electron. Inform. Technol. (in Chinese)*, *20*(7), 653–658. https://doi.org/10.11805/TKYDA2021316